Author Manuscript

Author Manuscript

Author Manuscript

Author Manuscript

HHS Public Access

Author manuscript

Cell Rep. Author manuscript; available in PMC 2021 November 23.

Published in final edited form as:

Cell Rep. 2021 November 02; 37(5): 109919. doi:10.1016/j.celrep.2021.109919.

Single-cell analysis of the human pancreas in type 2 diabetes using multi-spectral imaging mass cytometry

Minghui Wu[1,2,3,9], **Michelle Y.Y. Lee**[1,2,8,9], **Varun Bahl**[1,2], **Daniel Traum**[1,2], **Jonathan Schug**[1,2], **Irina Kusmartseva**[4], **Mark A. Atkinson**[4,5,7], **Guanjie Fan**[3,6], **HPAP Consortium**[7], **Klaus H. Kaestner**[1,2,10,*]

[1]Department of Genetics, University of Pennsylvania, Philadelphia, PA 19104, USA

[2]Institute for Diabetes, Obesity, and Metabolism, University of Pennsylvania, Philadelphia, PA 19104, USA

[3]The Second Clinical College, Guangzhou University of Chinese Medicine, Guangzhou, Guangdong 510720, China

[4]Departments of Pathology, Immunology, and Laboratory Medicine, University of Florida Diabetes Institute, Gainesville, FL 32610, USA

[5]Department of Pediatrics, University of Florida Diabetes Institute, College of Medicine, Gainesville, FL 32610, USA

[6]Department of Endocrinology, the Second Affiliated Hospital, Guangzhou University of Chinese Medicine, Guangzhou, Guangdong 510105, China

[7]The Human Pancreas Analysis Program (RRID:SCR_016202)

[8]Genomics and Computational Biology Graduate Group, University of Pennsylvania, Philadelphia, PA 19104, USA

[9]These authors contributed equally

[10]Lead contact

SUMMARY

Type 2 diabetes mellitus (T2D) is a chronic age-related disorder characterized by hyperglycemia due to the failure of pancreatic beta cells to compensate for increased insulin demand. Despite decades of research, the pathogenic mechanisms underlying T2D remain poorly defined. Here, we use imaging mass cytometry (IMC) with a panel of 34 antibodies to simultaneously quantify

This is an open access article under the CC BY-NC-ND license (http://creativecommons.org/licenses/by-nc-nd/4.0/).

*Correspondence: kaestner@pennmedicine.upenn.edu.

AUTHOR CONTRIBUTIONS

M.W. and D.T. performed imaging mass cytometry experiments; V.B. performed immunofluorescence staining; M.W., M.Y.Y.L., and J.S. performed computational and statistical data analysis; I.K., M.A.A., and K.H.K. wrote and edited the manuscript; and K.H.K. and G.F. supervised the study.

DECLARATION OF INTERESTS

The authors declare no competing interests.

SUPPLEMENTAL INFORMATION

Supplemental information can be found online at https://doi.org/10.1016/j.celrep.2021.109919.

Author Manuscript Author Manuscript Author Manuscript Author Manuscript

markers of pancreatic exocrine, islet, and immune cells and stromal components. We analyze over 2 million cells from 16 pancreata obtained from donors with T2D and 13 pancreata from age-similar non-diabetic controls. In the T2D pancreata, we observe significant alterations in islet architecture, endocrine cell composition, and immune cell constituents. Thus, both HLA-DR-positive CD8 T cells and macrophages are enriched intra-islet in the T2D pancreas. These efforts demonstrate the utility of IMC for investigating complex events at the cellular level in order to provide insights into the pathophysiology of T2D.

In brief

Wu et al. use an advanced imaging technique to profile two million cells within the pancreas of healthy people and those with T2D. They identify changes in tissue architecture and immune cell infiltration in the diabetic pancreas that help our understanding of this major health problem.

Graphical Abstract

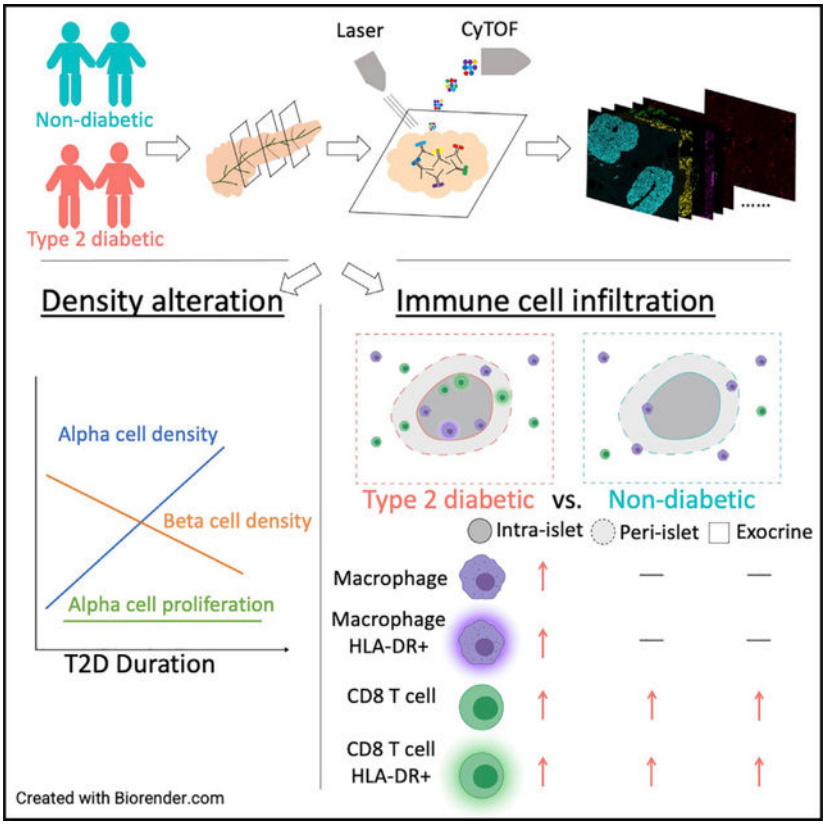

INTRODUCTION

The endocrine pancreas, although constituting only 1% to 2% of the organ’s mass, is highly effective at regulating blood glucose in a narrow physiological range (Atkinson et al., 2020; In’t Veld and Marichal, 2010). The insulin-producing beta cells, which comprise 20% to 60% of islet cells in the normal human pancreas (Wang et al., 2019), are able to adapt extensively to metabolic demand. However, this capacity is not without limits, with type 2

Author Manuscript Author Manuscript Author Manuscript Author Manuscript

diabetes (T2D) ensuing when insulin secretion becomes insufficient (DeFronzo et al., 2015). A seminal study by Deng and colleagues analyzed pancreatic islet structure and function in a large cohort of T2D cases (Deng et al., 2004); they noted that islet mass from the T2D pancreas was reduced (i.e., 50% of that of controls) and also reported that these islets were smaller and enriched for glucagon-producing alpha cells. Importantly, insulin secretion was impaired not only in terms of maximal output but also in glucose threshold, which shifted from 7 to 12 mM glucose (Deng et al., 2004).

Two potential mechanisms are frequently invoked to account for the beta cell failure observed with T2D, namely, beta cell "exhaustion" due to prolonged elevated insulin production and the associated endoplasmic reticulum (ER) stress (Bilekova et al., 2020; Kataoka and Noguchi, 2013) or a loss of beta cell mass through apoptosis following long-term exposure to high glucose/high lipid levels through a process termed "glucolipotoxicity." The latter mechanism is proposed to involve the Tolllike receptor (TLR)-mediated sensing of palmitate in beta cells, followed by chemokine production and recruitment of macrophages to the islet (Eguchi and Nagai, 2017). Indeed, islet inflammation has increasingly been proposed as the key player in beta cell dysfunction in T2D (reviewed in Eguchi and Nagai, 2017). Experimental support for this model derives from rodent studies (Eguchi et al., 2012; Masters et al., 2010; Westwell-Roper et al., 2014) as well as analyses of human pancreatic samples (Ehses et al., 2007; Kamata et al., 2014; Richardson et al., 2009). For example, an increased frequency of islet-resident macrophages was observed in leptin-deficient mice that become diabetic as a consequence of extreme hyperphagia (Ehses et al., 2007). Importantly, there was a shift from a predominantly M1 to M2 macrophage phenotype in this animal model (Cucak et al., 2014). Similarly, an elevated abundance of macrophages was also observed in human islets obtained from donors with T2D, both with and without amyloid deposition (Ehses et al., 2007; Richardson et al., 2009). The relevance of this observation to T2D pathogenesis in humans has been supported by clinical studies using interleukin-1 beta (IL-1β) receptor antagonists or neutralizing antibodies to IL-1β (Cavelti-Weder et al., 2012; Larsen et al., 2007). However, from these studies, it cannot be excluded that the observed improvements in glycemia and insulin secretion were the result of drug effects on peripheral tissues such as skeletal muscle, liver, or adipose tissue. Perhaps most importantly, these studies, although provocative and hypothesis generating in terms of their ability to address why T2D develops, were limited due to constraints in terms of complex data analysis and the technologies required to generate such information.

Indeed, determining the pathogenic events that occur in the T2D pancreas is critical not only for an improved understanding of the disorder's pathogenesis but also for the development of novel therapeutic approaches. However, the histopathological analysis of the human pancreas has been severely hampered by the fact that the pancreas cannot be easily or safely biopsied (Atkinson, 2014; Mueller et al., 1988). Thus, the vast majority of investigations have focused on rodent models such as the aforementioned leptin-deficient mouse or animals fed with various high fat/high sucrose diets in order to induce obesity and/or insulin resistance. Although the rodent models have the advantage of accessibility and ease of genetic manipulation, it is likely that they do not capture all aspects of islet failure in human T2D. In response to this issue, high-quality human pancreata, obtained from deceased organ

Author Manuscript Author Manuscript Author Manuscript Author Manuscript

donors, are increasingly being procured in limited numbers through organizations such as the Network for Pancreatic Organ donors with Diabetes (nPOD) (Campbell-Thompson et al., 2012) and, more recently, the NIH-supported Human Pancreas Analysis Program (HPAP; (Kaestner et al., 2019). Additionally, important data are being collected from metabolically phenotyped pancreatectomized patients as living donors (Wigger et al., 2021).

With these recent increases in tissue availability, opportunities exist to obtain information regarding islet cell subtyping, architectural frameworks, immune cell composition, and the identification of cell-cell interactions, as well as other cellular phenotypes that might contribute to the pathogenesis of T2D. Recent advances in combinatorial immunolabeling and multiplexed protein detection in situ have allowed for proteomic information that is not simply additive, but rather offers crucial insights into the cellular states and complex biological functions executed by different cell types within the islet environment. Here, in order to obtain such a multiplexed view of all critical cell types and states in the T2D pancreas, we used imaging mass cytometry (IMC) technology, which we have previously used successfully to analyze the pathogenesis of type 1 diabetes (T1D) (Wang et al., 2019). IMC applies metal-conjugated antibodies to label tissue sections that are subsequently ablated by a UV laser spot by spot. The resulting particle plumes are then transferred to a mass spectrometer for signal detection and quantification (Giesen et al., 2014). The precise laser registration in the sample ablation step allows for signal detection at a 1-μm resolution. More importantly, the discrete time-of-flight measurement of isotope mass in the mass spectrometry instrument facilitates multiplexing. In the following study, we used a panel of 34 antibodies to analyze pancreata from both control and patients with T2D and document striking changes in islet composition, immune cell infiltration, and cell-to-cell contacts within the islet microenvironment.

RESULTS AND DISCUSSION

Study overview

We used IMC for the co-registered determination of relative protein levels for 34 antigens relevant to human pancreas biology, including markers of all endocrine cell types (C-peptide of insulin, glucagon, somatostatin, PP, and ghrelin), and those specific for pancreatic ductal and acinar cells (Pan-Keratin, CD44, PDX1, Carbonic anhydrase II, and pS6), endothelial and stromal cells (CD31 and Nestin), extracellular matrix (Collagen Type 1), key transcription factors (PDX1 and NKX6.1), immune cells of the myeloid, lymphoid lineages (CD45, CD20, CD3, CD4, CD8, CD45RO, CD68, CD14, CD11b, HLA-DR, CD56, CD57, and Granzyme B [GnzB]), and major histocompatibility complex (MHC) class I and II proteins (HLA-ABC and HLA-DR) (see Table S1). After validation of our staining protocol using HPAP tissue samples, we selected our experimental cohorts from the nPOD archive to include 13 non-diabetic (ND) and 16 T2D cases (Table S2). Importantly, the two cohorts did not differ by sex distribution, age, or BMI (Table S2). Because of regional differences in islet composition and, possibly, disease presentation, we analyzed sections from the head, body, and tail of the pancreas separately, wherever available (Figure 1A). Figures 1B and 1C present three representative multi-color overlays each for a ND and a T2D pancreas obtained from the same IMC experiment. The selected images illustrate some of the major

Author Manuscript Author Manuscript Author Manuscript Author Manuscript

observations we quantitate below, namely, the relative loss of beta and gain of alpha cells, the increase in type 1 collagen deposition, and changes in the immune cell compartment in the T2D pancreas.

Image data processing and cell type profiling

To allow for quantitative analyses, we performed image processing to produce a table of cells with expression levels for the 34 antigens plus the 2 DNA channels in each region of interest (ROI) imaged, while retaining the location information for each cell (see STAR Methods). We then performed cell type calling to annotate the identity of each single cell. As the first step of image processing, we performed pixel-level processing to remove machine-induced artifacts such as streaks of extreme intensities and single "hot pixels." We then segmented each raw image into islets and individual cells, based on the strong pan-endocrine CD99 staining and DNA plus membrane staining, respectively. The expression of each protein was summarized by the mean pixel intensity across the segmented cell mask, turning the segmented cell images into a cell-protein expression table. We then performed cell-level compensation to mitigate any low-level spillovers observed between a given heavy metal isotope detection channel, its neighboring channels, and the channels containing potential oxidation products. Finally, the cells were annotated through two rounds of clustering, with the first round separating cells into the three major cell types endocrine, immune, and "other," while the second round assigned specific cell subtypes (see STAR Methods).

Overall cell type composition of the human pancreas

Through our IMC analysis of pancreatic tissue sections from 29 donors, we were able to assign cell types to 2,092,830 cells while retaining their positional information and relative protein expression levels. The heatmap in Figure 1D illustrates the results from cell type annotation. For example, cells with high levels of C-peptide, NKX6.1, PDX1, and CD99 were identified as beta cells, whereas cells expressing both Nestin and CD31 were defined as endothelial cells. For macrophages, CD8 T cells, and pancreatic ductal cells, we noted two subpopulations differing in their expression levels of HLA-DR, an MHC class II molecule (Figure 1D); we therefore considered them as two distinct cell states throughout the analyses.

Our approach of selecting ROIs based on the presence of at least one islet imparts a relative bias toward the endocrine compartment in our analysis, which reached approximately 10% of total cells analyzed (alpha, beta, delta, epsilon, and PP cells combined). Considering this information, we found that the overall composition of the pancreas was not dramatically different between the control and T2D groups, with 78.6% ± 8.7% of the ROIs comprised of exocrine (ductal and acinar) cells (Figures 1E and 1F). However, a subsequent, more detailed analysis of the alpha and beta cell density demonstrated that the frequency of beta cells was significantly decreased in the T2D pancreas (Figures 2A and 2C), with the strongest effect seen within the body of the organ (Figure 2A; $p < 0.01$), with the head and tail of the pancreas affected to a lesser extent (Figure 2A). The tissue density of alpha cells was reciprocally increased in the T2D pancreas, again with the strongest effect in the body of the organ (Figure 2B). Next, we analyzed the alpha-to-beta cell ratio, which we found to be

Author Manuscript Author Manuscript Author Manuscript Author Manuscript

significantly increased in the diabetic state (Figure 2C). Endocrine cell proportions by donor and region are quantified in Figure S1.

Changes in the T2D pancreas have been reported to be related to the duration of the disease (Chen et al., 2017); therefore, we analyzed our data to assess this possibility. Indeed, we observed a significant positive correlation between alpha cell density and T2D duration in the entire organ as well as in the body of the pancreas, along with a significant reduction in beta cell density that was notably associated with disease duration in the pancreas body (Figure S2).

Although the replication rates of human endocrine cells in adulthood are exceedingly low, they are higher in alpha cells than in beta or delta cells throughout life (Wang et al., 2019). To assess whether altered proliferation rates contribute to the shift in alpha and beta cell densities in T2D, we assessed for Ki67 status. In the ND pancreas, we observed the expected linear decrease in replication rates between 14 and 65 years of age, with an approximate 3-fold higher rate for alpha cells (Figure S3). In contrast, in the T2D tissues, proliferation rates of both alpha and beta cells were low even in younger individuals (Figure S3).

As noted earlier, we observed an increase in type I collagen deposition in the extracellular matrix of the T2D pancreas (Figures 1B and 1C). Therefore, we asked whether type 1 collagen deposition, a classical sign of fibrosis, is related to beta cell abundance. Although there was no correlation between the two parameters in the ND pancreas (data not shown), collagen density was significantly anti-correlated with beta cell density in T2D individuals (Figure 2D), suggesting a link between the fibrotic process and remaining beta cell mass.

Macrophages expressing intra-islet HLA class II are increased in T2D

Next, we turned our attention to the immune cell compartment within the pancreas. $CD68^+$ macrophages are present at the highest density within the exocrine pancreas and demonstrated an abundance of approximately 400 cells per mm^2, which did not differ overall between the T2D and ND samples, except in the head region (Figure 2F). However, when probing the positional information retained by IMC to quantify intra-islet macrophages, we observed a highly significant, nearly 2-fold increase in their abundance in tissues from T2D individuals, which was present in all three regions of the organ analyzed (Figure 2F). As mentioned previously, macrophages in the human pancreas can be divided into HLA class II high and low cells based on levels of HLA-DR. Although the $HLA\text{-}DR^{high}$ cells constituted between 15% and 65% of the total macrophage population in the pancreas (depending on donor and area), their relative abundance was increased throughout the organ in the T2D pancreas, with the greatest increase of approximately 2.1-fold intra-islet (Figure 2G).

CD8 T cells are increased in the T2D pancreas

Although the primary cause of T1D is autoimmunity, this is not the case for T2D. Nevertheless, islet inflammation has long been proposed to contribute to beta cell impairment in T2D (Ehses et al., 2007), but this proposal has sparse descriptions within the literature. Therefore, we analyzed the abundance and spatial distribution of CD8 T cells in the head, body, and tail of the pancreas in detail (Figure 3). We observed that the density

Author Manuscript Author Manuscript Author Manuscript Author Manuscript

of CD8 T cells was increased in the exocrine pancreas of donors with T2D, with trends in all three regions of the organ, which were statistically significant in the body (Figure 3B). This increase in CD8 T cell abundance was confirmed using standard immunofluorescence staining (Figure S5). Notably, the fold-change difference in CD8 T cell abundance between control and T2D was highest when we considered the intra- and peri-islet regions of the tissue. We also detected a small subset of CD8 T cells that stained positive for HLA-DR. Expression of MHC class II molecules on CD8 T cells is commonly used as a marker of activation (Ndhlovu et al., 2015). Interestingly, we observed that HLA-DR^{high} CD8 T cells were increased significantly in the T2D pancreas and elevated up to 2.9-fold in the intraislet region (Figure 3C).

Neighborhood analysis of IMC data

The retention of spatial information following segmentation and cell type identification in IMC enabled neighborhood analyses for the more than 2 million cells captured in our study. Figure 4A illustrates the accuracy of our cell type annotation pipeline. On the left of this figure, we show an overlay of an ROI with seven markers that are expressed in the major epithelial cells of the pancreas, and the image on the right displays the 14 cell types identified after our cell type profiling. Having established the high degree of similarity between the actual image and post-segmentation rendering, we proceeded to perform HistoCAT neighborhood analysis to examine the frequencies of specific cell-cell interactions (Schapiro et al., 2017) as schematized in Figure 4B and Figure S4. Each cell type was considered as the “query cell,” and the frequency of every other cell type being in its neighborhood was recorded. Next, we compared the frequency with a null distribution and calculated an enrichment score representing the deviation from the null (see STAR Methods). Following this step, we compared the neighborhood enrichment between ND and T2D, as summarized in the heatmap in Figure 4C. Shown on the left are the labels of the query cells (row labels), and shown on the bottom are the labels of the neighborhood cell types. Plotted are the differences in specific cell-cell interactions. The shading of each square indicates whether this interaction is enriched in the pancreas from control or patients with T2D, and black boxes highlight those demonstrating statistical significance. Through this analysis, we determined that CD8 T cells and CD68^{+} macrophages are more likely to be in contact with islet beta cells, whereas macrophages are less likely to be near acinar cells in T2D.

In summary, we have demonstrated the power of IMC for the analysis of the histopathological changes in human T2D and, with these data, brought insights regarding the pancreas in T2D, which are efforts that provide important clues into the disorder’s pathogenesis. We have confirmed the relative loss of beta cells and increase in alpha cells in T2D, a facet of the disease phenotype that is dependent on disease duration. We discovered that the aging-dependent decline in islet endocrine cell proliferation is accelerated in individuals with T2D (Figure S3). These findings suggest that the relative increase in alpha cell number in T2D is not driven by higher proliferation rates, which leaves *trans*-differentiation from another cell type or de novo generation from adult endocrine progenitor cells yet to be defined as the remaining likely options. Finally, our efforts also noted a negative correlation between islet collagen area and beta cell density, providing

Author Manuscript Author Manuscript Author Manuscript Author Manuscript

further evidence that fibrosis might play a contributing role in beta cell loss in T2D. An increased abundance of islet-resident macrophages was first reported by the Donath group in 2007, with *in vitro* experiments suggesting that islets incubated with very high glucose and palmitate concentrations could secrete pro-inflammatory cytokines and chemokines, which could in turn stimulate monocyte/macrophage recruitment (Ehses et al., 2007). Here, we confirmed and extended these findings by demonstrating not only that intraislet macrophage density is increased in T2D but also that a subset of these expressed high levels of HLA-DR, the significance of which awaits further analysis. The presence of CD8 T cells in the T2D pancreas has also been reported previously, but with the conclusion that CD8 T cells are increased only in the exocrine pancreas but not in islets (Rodriguez-Calvo et al., 2014). In addition, when using fluorescence-activated cell sorting (FACS) analysis on isolated islets, Butcher and colleagues found no change in CD3 T cell abundance in T2D (Butcher et al., 2014), although it is possible that this approach missed leukocytes that migrated out of the islet during isolation. In contrast, we observed an increased density of CD8 T cells within islets, and this relative shift of CD8 T cells from the exocrine pancreas to the islet in T2D was confirmed by our neighborhood analysis (Figure 4B). Interestingly a subset of islet-resident CD8 T cells were positive for HLA-DR, a common marker of T cell activation (Ndhlovu et al., 2015), and the density of these islet-resident $CD8^{+}HLA\text{-}DR^{+}$ cells was also increased in T2D. These findings suggest that activated CD8 T cells could contribute to islet inflammation in human T2D.

Limitations of study

We note that there are several potential limitations to our study. Although we were able to analyze a sufficient number of cases to define statistically significant differences between ND and T2D pancreata in terms of islet composition, immune cell infiltration, and cellular neighborhoods, our efforts were unfortunately underpowered to analyze heterogeneity among the patients with T2D. Disease heterogeneity among the clinical presentation of patients with T2D is increasing recognized, with several classification systems recently proposed (Ahlqvist et al., 2020). Future studies should include organ donors typed for future consensus subclassifications of T2D to study this issue further.

Beyond this issue, there were additional limitations related to the IMC platform. Although this technology enables the simultaneous detection of several dozen antigens and is not plagued by issues of tissue auto-fluorescence often seen in immunofluorescence approaches, IMC can result in low sensitivity for some proteins because “exposure time” cannot be increased, as can be performed for fluorescence-based imaging platforms. In addition, subcellular location analysis is limited because each pixel has 1-mm squared dimensions. Finally, IMC destroys the tissue in the laser ablation process, and therefore, additional orthogonal experiments cannot be performed.

Author Manuscript Author Manuscript Author Manuscript Author Manuscript

STAR⋆METHODS

RESOURCE AVAILABILITY

Lead contact—Further information and requests for resources and reagents should be directed to and will be fulfilled by the lead contact, Klaus Kaestner (kaestner@pennmedicine.upenn.edu).

Materials availability—Metal-conjugated antibodies generated in this study will be made available on request, but we may require a payment and/or a completed Materials Transfer Agreement if there is potential for commercial application.

Data and code availability—Raw image data have been deposited at nPOD website (https://www.jdrfnpod.org) and are publicly available as of the date of publication. All original code has been deposited at https://github.com/Kaestner-Lab/T2D_IMC and is publicly available as of the date of publication. The DOI is listed in the key resources table. Any additional information required to reanalyze the data reported in this paper is available from the lead contact upon request

EXPERIMENTAL MODEL AND SUBJECT DETAILS

The pancreas tissue samples were obtained from the Network for Pancreatic Organ Donors with Diabetes (nPOD, https://www.jdrfnpod.org/) under IRB approval by the University of Florida. Donor clinical information was obtained from nPOD and T2D diagnosis followed ADA guidelines. Please refer to Table S2 in this section for information on donor age/gender.

METHOD DETAILS

Antibody Panel and labeling—20 of 34 conjugated antibodies were purchased from FluidigmR (https://www.fluidigm.com). The other 14 unconjugated antibodies were obtained from different vendors (Table S1) and conjugated to lanthanide metals using the MaxPar X8 Multimetal Labeling Kit (Fluidigm) according to the manufacturer's protocol. Antibodies were diluted with 0.5% BSA in PBS.

Tissue staining and image acquisition—Five to eight mm formalin-fixed paraffin-embedded pancreas sections were stained with a cocktail of 34 antibodies (Table S1). Tissues were de-paraffined with xylene for 30 minutes and rehydrated in the sequential ethanol from 100% to 70% with changes every 5 minutes. After transfer to ddH_2O for 5 minutes, we performed epitope retrieval in a decloaking chamber with HIER buffer (10mM Tris, 1mM EDTA, pH9.2) for 30 minutes at 95C. Tissue sections were allowed to cool to room temperature in HIER buffer and then transferred to PBS for 20 minutes. After blocking in 3% BSA for 1 hour, the tissues were stained with the antibody cocktail at 4C overnight. The next day, the tissues were labeled by 1:400 dilution of Ir-intercalator solution (Fluidigm 201192B) in PBS for 30 minutes to label nuclei. Slides were washed in PBS two times for 5 minutes, dipped 2 minutes in ddH_2O and airdried before IMC acquisition.

Author Manuscript Author Manuscript Author Manuscript Author Manuscript

Following Fluidigm's operation instruction and daily tuning we acquired the IMC images at a laser frequency of 200 Hz using Fluidigm's Hyperion instrument. 1,000 μm × 1,000 μm regions around islets were selected based on analysis of adjacent H/E stained sections. Finally, we converted the mcd files to tiff images using Fluidigm's MCD viewer.

Image processing—We captured a total of 260 images (regions of interest of 1,000 μm × 1,000 μm) from our cohort of 16 T2D and 13 non-diabetic donors. Prior to signal quantification, streaks of pixels with extreme intensity were detected based on two background channels (Iridium 113 and Iridium 115) and were removed using an approach adopted from Wang et al. (2019). Specifically, a 5×5 grid was used to search for pixels with intensity among the 2% of the whole image and greater than 2× median intensity of the grid (the median was calculated excluding the center row). A list of pixels fulfilling this requirement in the first two background channels were tested again in the following protein channels and pixels with value greater than 5x the median intensity of the 5×5 grid, were replaced with the median intensity. Lastly, single "hot pixels" with intensity greater than 50 (intensity units) of the maximum value in its 3×3 neighborhood were replaced with the local maximum, using a CellProfiler plugin (Zanotelli et al., 2020).

Cell segmentation—Cells masks were generated following a published pipeline (Zanotelli and Bodenmiller, 2017). First, CD99 was used to detect cell membranes of endocrine and exocrine cells. Due to the large difference in CD99 intensity between the two cell populations, the 'Enhance Local Contrast (CLAHE)' function in Fiji (Schindelin et al., 2012) was applied to CD99 channel (blocksize = 39, histogram = 256, maximum = 40, mask = 'none'). Second, four channels were selected for cell segmentation: CD45, CD68, enhanced CD99, Iridium 193 (the Iridium DNA intercalator labels nuclei). Images were enlarged by 2-fold and converted to the h5 format. H5 files were then imported into Ilastik v1.3.3 (Berg et al., 2019) for pixel classification training. Specifically, a Random Forest model was trained using the 37 default features to classify pixels into one of three classes: nuclei, membrane, or background. Four images were labeled manually for training, then the classifier was applied onto the rest of images. The outputs of Ilastik were three probability maps, one for each class. The nuclei probability map was used to detect primary object (nuclei) in CellProfiler (Carpenter et al., 2006) with the minimum cross entropy method. Primary objects with an area of less than 5 pixels were filtered out. Secondary objects were identified using the Distance – B method. Specifically, primary objects recognized in the previous step were expanded with guidance of the cell membrane probability map, with maximum expansion constrained as 10 pixels. Resulting cell masks were resized by 0.5-fold to the original scale and cells with area less than 25 pixels were removed. Lastly, the cell masks were used to measure mean protein expression for each channel and each cell in the original IMC images post pre-processing steps. The x and y coordinate of all cells in the image were also recorded.

Spillover compensation—Signal crosstalk between channels were compensated using the functions from CATALYST R package (v.1.12.2) (Chevrier et al., 2018) based on the isotope purity matrix provided by Fluidigm.

Author Manuscript Author Manuscript Author Manuscript Author Manuscript

Islet segmentation and measurement—We employed a similar workflow for islet segmentation. Specifically, a separate model was trained to generate islet probability maps based on the CD99 channel. The probability maps were segmented into the islet masks using CellProfiler using a similar process as described for cell masks. Islets masks were expected to have a diameter greater than 10 μm and size greater than 50 μm^2. We determined islet related measurements with CellProfiler as well. Peri-islet regions were identified as 30 μm-wide region extending from the boundary of islet mask, while the rest of the images (not intra-islet or peri-islet) were labeled as exocrine. For islet collagen percentage, we expanded the islet mask by 50mm, segmented collagen positive regions, and quantified the percentage of expanded islet area positive for collagen signal.

Immunofluorescence (IF) staining—Twenty-three slides from the body of the pancreas were analyzed for CD99 and CD8 expression using immunofluorescent staining. Five to eight μm formalin-fixed and paraffin embedded (FFPE) pancreas tissue sections were deparaffinized in xylene and rehydrated through a series of ethanol washes, followed by antigen retrieval for 30 minutes in Tris/EDTA buffer (pH 9.0). Sections were blocked using 10% FBS/1X PBS, and primary antibodies were diluted in 10% FBS/1X PBS and applied overnight at 4C. The next day, sections were washed in PBS and incubated with the appropriate secondary antibodies diluted in 10% FBS/1X PBS for 2-h at RT. Primary and secondary antisera information is provided in Tables S1 and S2, respectively. Hoechst 33342 (Thermo #H3570) was used to counterstain nuclei. Staining was scanned using a Keyence BZ-X800 fluorescence microscope. Fluorescence staining of CD8 and DAPI were used to segment CD8 T cells, and CD99 was used to identify islets. Two regions of interests were captured from each slide, resulting in a total of 46 images.

CD8 T cell and islet segmentation for immunofluorescence images—Ilastik v1.3.3 (Berg et al., 2019) was used to identify CD8 T cells. Specifically, a 500-pixel × 500-pixel region was cropped randomly from each image and nuclei surrounded by CD8 expression were labeled as CD8 T cell signal. After labeling, a probability map for every pixel was generated and pixels with greater than 0.5 for CD8 T cell signal were connected, resulted in segmented CD8 T cells. Cells with less than 5 pixels in area were filtered out. Islet masks were generated using a similar approach as the CD8 T cells, except 20 full-size images were used for training. Segmented islet masks generated by Ilastik were then filtered using CellProfiler to remove islets with a size less than 50 μm^2 and a radius less than 5 μm. The FillObject module was also used in CellProfiler to fill holes in segmented islet mask. Annotation of peri-islet and exocrine region were performed similarly as described in “Islet segmentation and measurement.” The resolution of IF is different from that of IMC. Thus, each pixel in our IF images had a size of 0.77 μm × 0.77 μm, therefore, the distance measurements were scaled accordingly.

QUANTIFICATION AND STATISTICAL ANALYSIS

Data transformation and normalization—We normalized mean pixel intensity of each target channel for each cell as described below before downstream quantitative analyses. First, we transformed the raw mean pixel intensity data by $\log_2$ (mean intensity+1). For most antibody targets, the most common cell signal value corresponds to cells that do not express

Author Manuscript Author Manuscript Author Manuscript Author Manuscript

the target. Thus, for each image, we identify the most frequent signal value mode, S_0, using the highest peak in a smoothed estimate of the distribution of the log transformed signal values (S) for each channel (R function density [S, n = 2^16]). Subsequently, we calculated the normalized value $S_n = S - S_0$ and set $S_n < 0$ to 0. Lastly, S_n is pooled across all images and clipped to the 99.99th percentile value for each channel to remove any outliers.

Clustering and meta clustering—We performed clustering following the FlowSOM workflow (Van Gassen et al., 2015). Cells with normalized protein mean expression were clustered in two steps. First, we grouped all cells into 225 clusters using a self-organizing map. Markers used for clustering in this stage were selected based on a high signal-to-noise ratio and their information content for cell type calling as follows: C-peptide, Glucagon, Somatostatin, PP, PDX.1, NKX6.1, Ghrelin, CD99, Carbonic Anhydrase 2, NF-κb, CD44, Nestin, CD31, CD56, CD57, HLA.DR, β-Actin, HLA.ABC, phospho-S6(pS6), Foxp3, p16, CD8, CD3, CD45RO, CD4, CD45, Granzyme B, CD68, CD14, CD20. Next, we combined the 225 groups into 40 clusters using the 'MetaClustering_consensus' function in the FlowSOM package. Next, the 40 clusters were grouped manually into 3 major cell types: 'endocrine', 'immune', and 'other' based on the mean and distribution of the marker proteins. In the second step, each cell type was reclustered using the same workflow as in the first step. Cell were divided into 225 groups with a self-organizing map and recombined into 50 clusters. Markers used were the same with the first stage except that we excluded CD99 for endocrine clusters. The resulting 150 clusters, 50 for each major cell type were annotated based on the distribution and mean of protein expression. For ambiguous clusters, images were inspected to determine the most appropriate cell type on the basis of cell location and morphology.

Neighborhood analysis—We adopted the HistoCAT neighborhood analysis to examine cell-cell interaction difference between conditions (Schapiro et al., 2017). We used the R implementation available on Github, "BodenmillerGroup/neighbouRhood." Cells were considered as neighbors if their centers were less than 20 pixels apart. For each ROI, we calculated an interaction score between two cell types, with one cell type (A) being the query cell and the other cell type (B) being the neighboring cell. Specifically, IAB is the average number of cell type B (neighboring cell) in the neighborhood of cell type A (center cell). Then, a permutation was employed by shuffling cell labels and thus resulted in a null distribution, assuming that all cells interacted randomly. We used 100 rounds of permutation and calculated a mean for each type of interaction. We then calculated an enrichment score, the difference between observed interaction and expected interaction under the null model. Lastly, we used permutation tests with 5,000 iterations to compare the enrichment score between T2D and ND, and Benjamini-Hochberg adjustment for multiple testing was applied to the resulting p values. An interaction was accepted as significantly enriched in one condition if the adjusted p value < 0.05. In all the images, the boundary cells were excluded from the neighborhood calculation because they do not represent a true neighborhood due to image cutoff.

Statistical methods—For Figures 2A–2C, 2F, 2G, 3B, 3C, and S5, Mann-Whitney test with p % 0.05 was used for statistical testing. For data associated with Figures 2D, S2A,

Author Manuscript Author Manuscript Author Manuscript Author Manuscript

S2B, S3A, and S3B, statistical analyses were performed with linear regression t test. For Figure 4B, Benjamini-Hochberg adjustment for multiple testing was applied. For Table S2, the chi-square test was used to compare the sex distribution, the unpaired t test was used to compare the age and BMI. P value < 0.05 is statistically significant. P values were represented as follows: *p < 0.05; **, p < 0.01; ***, p < 0.001, **** p < 0.0001.

Supplementary Material

Refer to Web version on PubMed Central for supplementary material.

ACKNOWLEDGMENTS

We thank Dr. Mingyao Li, Dr. Ayano Kondo, and Dr. Long Gao for advice on data analysis. Funding was provided by NIH grants U01 DK123594 (to K.H.K.) and P01 AI42288 (to M.A.A.). This research was performed with the support of the Network for Pancreatic Organ donors with Diabetes (nPOD; RRID:SCR_014641), a collaborative type 1 diabetes research project sponsored by JDRF (nPOD: 5-SRA-2018–557-Q-R), and The Leona M. & Harry B. Helmsley Charitable Trust (grant number 2018PG-T1D053).

REFERENCES

Ahlqvist E, Prasad RB, and Groop L (2020). Subtypes of Type 2 Diabetes Determined From Clinical Parameters. Diabetes 69, 2086–2093. [PubMed: 32843567]

Atkinson MA (2014). Pancreatic biopsies in type 1 diabetes: revisiting the myth of Pandora's box. Diabetologia 57, 656–659. [PubMed: 24442510]

Atkinson MA, Campbell-Thompson M, Kusmartseva I, and Kaestner KH (2020). Organisation of the human pancreas in health and in diabetes. Diabetologia 63, 1966–1973. [PubMed: 32894306]

Berg S, Kutra D, Kroeger T, Straehle CN, Kausler BX, Haubold C, Schiegg M, Ales J, Beier T, Rudy M, et al. (2019). ilastik: interactive machine learning for (bio)image analysis. Nat. Methods 16, 1226–1232. [PubMed: 31570887]

Bilekova S, Sachs S, and Lickert H (2020). Pharmacological Targeting of Endoplasmic Reticulum Stress in Pancreatic Beta Cells. Trends Pharmacol. Sci 42, 85–95, . [PubMed: 33353789]

Butcher MJ, Hallinger D, Garcia E, Machida Y, Chakrabarti S, Nadler J, Galkina EV, and Imai Y (2014). Association of proinflammatory cytokines and islet resident leucocytes with islet dysfunction in type 2 diabetes. Diabetologia 57, 491–501. [PubMed: 24429578]

Campbell-Thompson M, Wasserfall C, Kaddis J, Albanese-O'Neill A, Staeva T, Nierras C, Moraski J, Rowe P, Gianani R, Eisenbarth G, et al. (2012). Network for Pancreatic Organ Donors with Diabetes (nPOD): developing a tissue biobank for type 1 diabetes. Diabetes Metab. Res. Rev 28, 608–617. [PubMed: 22585677]

Carpenter AE, Jones TR, Lamprecht MR, Clarke C, Kang IH, Friman O, Guertin DA, Chang JH, Lindquist RA, Moffat J, et al. (2006). CellProfiler: image analysis software for identifying and quantifying cell phenotypes. Genome Biol. 7, R100. [PubMed: 17076895]

Cavelti-Weder C, Babians-Brunner A, Keller C, Stahel MA, Kurz-Levin M, Zayed H, Solinger AM, Mandrup-Poulsen T, Dinarello CA, and Donath MY (2012). Effects of gevokizumab on glycemia and inflammatory markers in type 2 diabetes. Diabetes Care 35, 1654–1662. [PubMed: 22699287]

Chen C, Cohrs CM, Stertmann J, Bozsak R, and Speier S (2017). Human beta cell mass and function in diabetes: Recent advances in knowledge and technologies to understand disease pathogenesis. Mol. Metab. 6, 943–957. [PubMed: 28951820]

Chevrier S, Crowell HL, Zanotelli VRT, Engler S, Robinson MD, and Bodenmiller B (2018). Compensation of Signal Spillover in Suspension and Imaging Mass Cytometry. Cell Syst. 6, 612–620.e5. [PubMed: 29605184]

Cucak H, Grunnet LG, and Rosendahl A (2014). Accumulation of M1-like macrophages in type 2 diabetic islets is followed by a systemic shift in macrophage polarization. J. Leukoc. Biol. 95, 149–160. [PubMed: 24009176]

Author Manuscript Author Manuscript Author Manuscript Author Manuscript

DeFronzo RA, Ferrannini E, Groop L, Henry RR, Herman WH, Holst JJ, Hu FB, Kahn CR, Raz I, Shulman GI, et al. (2015). Type 2 diabetes mellitus. Nat. Rev. Dis. Primers 1, 15019. [PubMed: 27189025]

Deng S, Vatamaniuk M, Huang X, Doliba N, Lian MM, Frank A, Velidedeoglu E, Desai NM, Koeberlein B, Wolf B, et al. (2004). Structural and functional abnormalities in the islets isolated from type 2 diabetic subjects. Diabetes 53, 624–632. [PubMed: 14988246]

Eguchi K, and Nagai R (2017). Islet inflammation in type 2 diabetes and physiology. J. Clin. Invest. 127, 14–23. [PubMed: 28045399]

Eguchi K, Manabe I, Oishi-Tanaka Y, Ohsugi M, Kono N, Ogata F, Yagi N, Ohto U, Kimoto M, Miyake K, et al. (2012). Saturated fatty acid and TLR signaling link β cell dysfunction and islet inflammation. Cell Metab. 15, 518–533. [PubMed: 22465073]

Ehses JA, Perren A, Eppler E, Ribaux P, Pospisilik JA, Maor-Cahn R, Gueripel X, Ellingsgaard H, Schneider MK, Biollaz G, et al. (2007). Increased number of islet-associated macrophages in type 2 diabetes. Diabetes 56, 2356–2370. [PubMed: 17579207]

Giesen C, Wang HA, Schapiro D, Zivanovic N, Jacobs A, Hattendorf B, Schüffler PJ, Grolimund D, Buhmann JM, Brandt S, et al. (2014). Highly multiplexed imaging of tumor tissues with subcellular resolution by mass cytometry. Nat. Methods 11, 417–422. [PubMed: 24584193]

In't Veld P, and Marichal M (2010). Microscopic anatomy of the human islet of Langerhans. Adv. Exp. Med. Biol. 654, 1–19. [PubMed: 20217491]

Kaestner KH, Powers AC, Naji A, and Atkinson MA; HPAP Consortium (2019). NIH Initiative to Improve Understanding of the Pancreas, Islet, and Autoimmunity in Type 1 Diabetes: The Human Pancreas Analysis Program (HPAP). Diabetes 68, 1394–1402. [PubMed: 31127054]

Kamata K, Mizukami H, Inaba W, Tsuboi K, Tateishi Y, Yoshida T, and Yagihashi S (2014). Islet amyloid with macrophage migration correlates with augmented β-cell deficits in type 2 diabetic patients. Amyloid 21, 191–201. [PubMed: 25007035]

Kataoka HU, and Noguchi H (2013). ER Stress and β-Cell Pathogenesis of Type 1 and Type 2 Diabetes and Islet Transplantation. Cell Med. 5, 53–57. [PubMed: 26858865]

Larsen CM, Faulenbach M, Vaag A, Vølund A, Ehses JA, Seifert B, Mandrup-Poulsen T, and Donath MY (2007). Interleukin-1-receptor antagonist in type 2 diabetes mellitus. N. Engl. J. Med. 356, 1517–1526. [PubMed: 17429083]

Masters SL, Dunne A, Subramanian SL, Hull RL, Tannahill GM, Sharp FA, Becker C, Franchi L, Yoshihara E, Chen Z, et al. (2010). Activation of the NLRP3 inflammasome by islet amyloid polypeptide provides a mechanism for enhanced IL-1b in type 2 diabetes. Nat. Immunol. 11, 897–904. [PubMed: 20835230]

Mueller PR, Miketic LM, Simeone JF, Silverman SG, Saini S, Wittenberg J, Hahn PF, Steiner E, and Forman BH (1988). Severe acute pancreatitis after percutaneous biopsy of the pancreas. AJR Am. J. Roentgenol. 151, 493–494. [PubMed: 3261508]

Ndhlovu ZM, Kamya P, Mewalal N, Kløverpris HN, Nkosi T, Pretorius K, Laher F, Ogunshola F, Chopera D, Shekhar K, et al. (2015). Magnitude and Kinetics of CD8+ T Cell Activation during Hyperacute HIV Infection Impact Viral Set Point. Immunity 43, 591–604. [PubMed: 26362266]

Pau G, Fuchs F, Sklyar O, Boutros M, and Huber W (2010). EBImage— an R package for image processing with applications to cellular phenotypes. Bioinformatics 26, 979–981. [PubMed: 20338898]

Richardson SJ, Willcox A, Bone AJ, Foulis AK, and Morgan NG (2009). Islet-associated macrophages in type 2 diabetes. Diabetologia 52, 1686–1688. [PubMed: 19504085]

Rodriguez-Calvo T, Ekwall O, Amirian N, Zapardiel-Gonzalo J, and von Herrath MG (2014). Increased immune cell infiltration of the exocrine pancreas: a possible contribution to the pathogenesis of type 1 diabetes. Diabetes 63, 3880–3890. [PubMed: 24947367]

Schapiro D, Jackson HW, Raghuraman S, Fischer JR, Zanotelli VRT, Schulz D, Giesen C, Catena R, Varga Z, and Bodenmiller B (2017). histoCAT: analysis of cell phenotypes and interactions in multiplex image cytometry data. Nat. Methods 14, 873–876. [PubMed: 28783155]

Schindelin J, Arganda-Carreras I, Frise E, Kaynig V, Longair M, Pietzsch T, Preibisch S, Rueden C, Saalfeld S, Schmid B, et al. (2012). Fiji: an open-source platform for biological-image analysis. Nat. Methods 9, 676–682. [PubMed: 22743772]

Author Manuscript Author Manuscript Author Manuscript Author Manuscript

Van Gassen S, Callebaut B, Van Helden MJ, Lambrecht BN, Demeester P, Dhaene T, and Saeys Y (2015). FlowSOM: Using self-organizing maps for visualization and interpretation of cytometry data. Cytometry A 87, 636–645. [PubMed: 25573116]

Wang YJ, Traum D, Schug J, Gao L, Liu C, Atkinson MA, Powers AC, Feldman MD, Naji A, Chang KM, and Kaestner KH; HPAP Consortium (2019). Multiplexed In Situ Imaging Mass Cytometry Analysis of the Human Endocrine Pancreas and Immune System in Type 1 Diabetes. Cell Metab. 29, 769–783.e4. [PubMed: 30713110]

Westwell-Roper CY, Ehses JA, and Verchere CB (2014). Resident macrophages mediate islet amyloid polypeptide-induced islet IL-1β production and β-cell dysfunction. Diabetes 63, 1698–1711. [PubMed: 24222351]

Wigger L, Barovic M, Brunner AD, Marzetta F, Schöniger E, Mehl F, Kipke N, Friedland D, Burdet F, Kessler C, et al. (2021). Multi-omics profiling of living human pancreatic islet donors reveals heterogeneous beta cell trajectories towards type 2 diabetes. Nat. Metab 3, 1017–1031. [PubMed: 34183850]

Zanotelli VR, and Bodenmiller B (2017). ImcSegmentationPipeline: A pixel-classification based multiplexed image segmentation pipeline (v0.9). Zenodo, https://zenodo.org/record/3841961#.YW85Li2ZNTY.

Zanotelli VR, Windhager J, and Rau R (2020). BodenmillerGroup/ImcPluginsCP: Bugfixes and new modules (Version cp3_v1.2). Zenodo, https://github.com/BodenmillerGroup/ImcPluginsCP.

Author Manuscript Author Manuscript Author Manuscript Author Manuscript

Highlights

- Imaging mass cytometry profiles of the T2D pancreas with 34 antibodies
- There of is a relative loss beta and gain of alpha cells in the T2D pancreas
- Advanced neighborhood analysis finds increased macrophage/beta cell contacts in T2D
- Activated HLA-DR-positive CD8 T cells are enriched in the T2D islet

Author Manuscript Author Manuscript Author Manuscript Author Manuscript

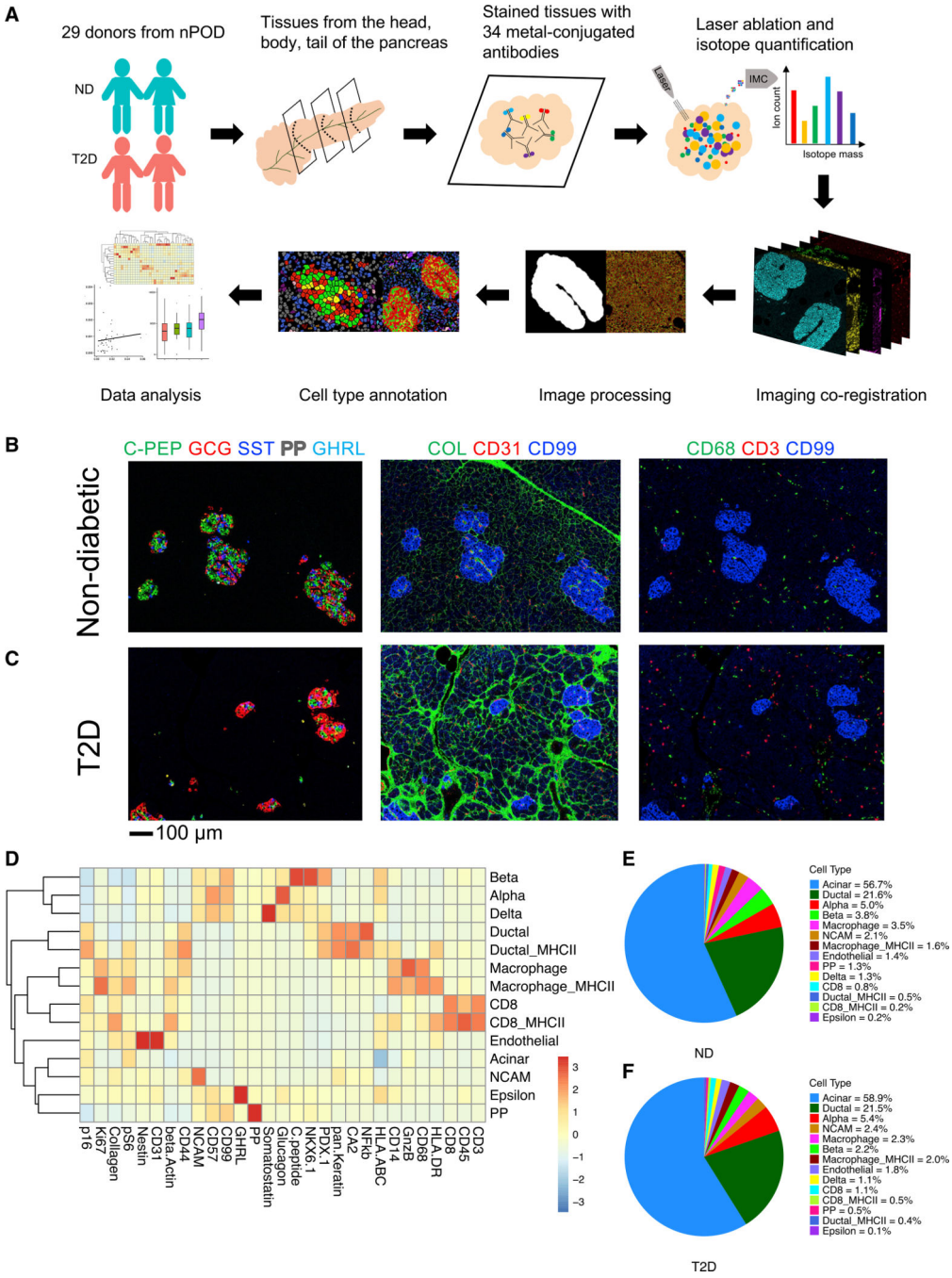

Figure 1. Overview of the imaging mass cytometry study of the human pancreas

(A) Imaging mass cytometry workflow.

(B and C) Representative multiple-channel image overlays of non-diabetic (ND) (B) and type 2 diabetic (T2D) (C) pancreas. From left to right, displayed channels are as follows: on the left image, C-peptide (green), glucagon (red), somatostatin (blue), PP (white), and Ghrelin (cyan); in the middle image, collagen (green), CD31 (red) and CD99 (blue); on the right image, CD68 (green), CD3 (red), and CD99 (blue).

Author Manuscript Author Manuscript Author Manuscript Author Manuscript

(D) Heatmap of mean expression values of each protein in each cell type. Input data are mean level of each protein in each cell type. Color indicates Z- score. The x-axis labels are the proteins, and the yaxis label are the cell types.
(E and F) The proportion of each cell type in ND (E) and T2D (F).
See also Tables S1 and S2 and Figure S1.

Author Manuscript
Author Manuscript
Author Manuscript
Author Manuscript

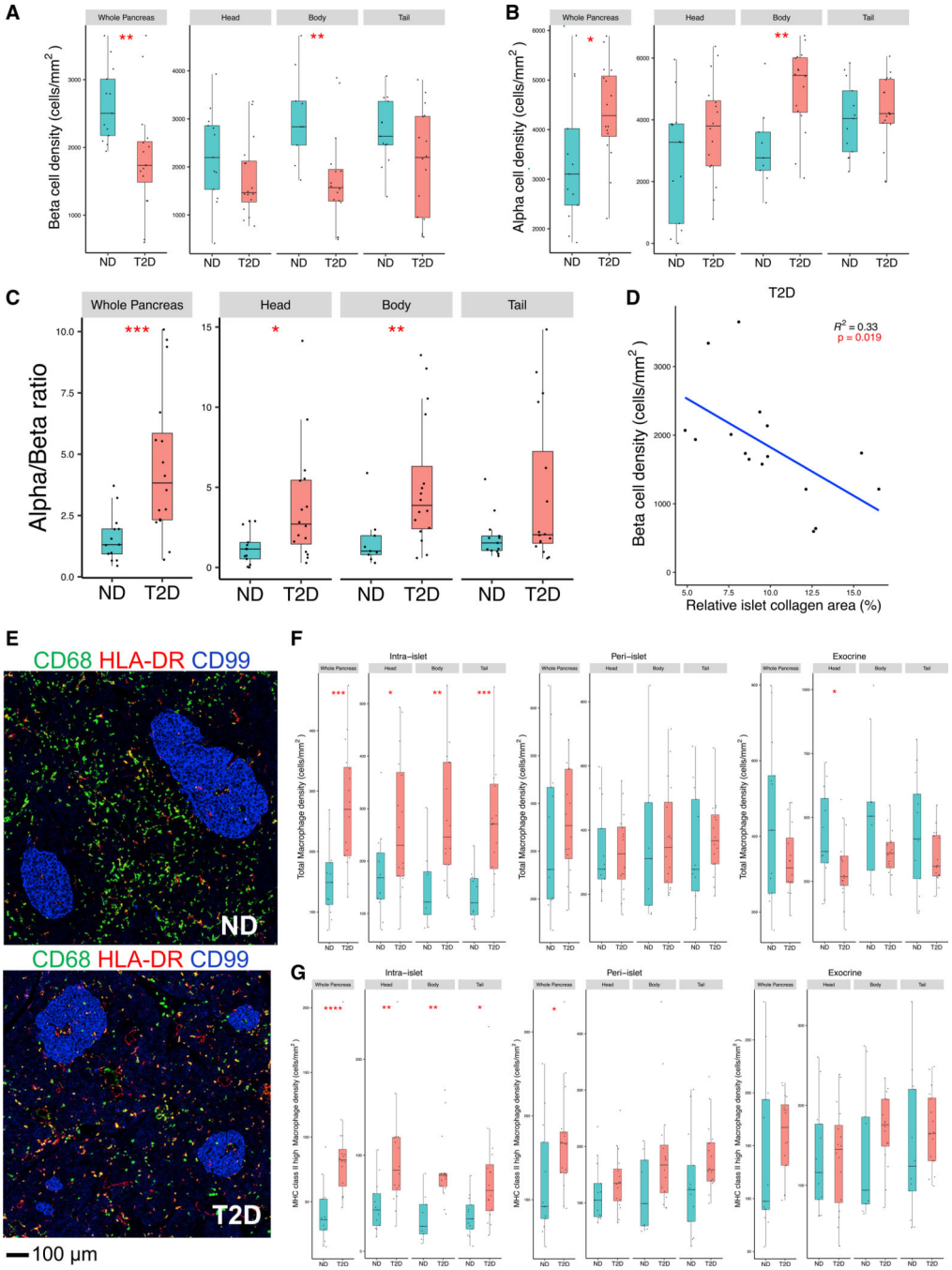

Figure 2. Altered alpha and beta cell as well as macrophage distribution in the T2D pancreas

(A) Boxplots showing the density of beta cells in the human pancreas, either for the whole organ or separately for the head, body, or tail. Each dot represents the mean density of each donor. The black line inside of the boxplot indicates the median density, and the whisker shows ±1.53 interquartile range. ND, n = 13; T2D, n = 16. *p < 0.05, **p < 0.01. Mann-Whitney U test.

(B) Boxplots showing the density of alpha cells in the human pancreas, analogous to (A) *p < 0.05, **p < 0.01. Mann-Whitney U test.

Author Manuscript Author Manuscript Author Manuscript Author Manuscript

(C) Boxplots of the alpha cell/beta cell ratio in the ND and T2D pancreas, either for the whole organ or separately for the head, body, or tail. Each dot represents the mean ratio of each donor. The black line inside of the boxplot indicates the median ratio, and the whisker shows ±1.53 interquartile range. ND, n = 13; T2D, n = 16. **p < 0.05, **p < 0.01, ***p < 0.001. Mann-Whitney U test.

(D) Beta cell density is inversely proportional to type 1 collagen deposition in the T2D pancreas (n = 16). Islet collagen is measured by the percentage of expanded islet area (islet region + within 50 mm from islet boundary) with positive collagen signal. Statistical significance was tested by linear regression t test. Each dot demonstrates one donor.

(E) Representative image of $CD68^{+}$ macrophages with or without HLA-DR expression in the pancreas from ND (above) and T2D (below) organ donor. Islets outlined by CD99 (blue).

(F) Boxplots showing the total macrophage density intra-islet, peri-islet, or in the exocrine pancreas. Data are presented for the whole pancreas and separately for head, body, and tail of the organ. Each dot represents the mean density of each donor. The black line inside of the boxplot indicates the median density, and the whisker shows ±1.53× interquartile range. ND, n = 13; T2D, n = 16. *p < 0.05, **p < 0.01. Mann-Whitney U test.

(G) Boxplots showing $HLA\text{-}DR^{high}$ macrophage density intra-islet, peri-islet, or in the exocrine pancreas. Data are presented for the whole pancreas and separately for head, body, and tail of the organ. Each dot represents the mean density of each donor. The black line inside of the boxplot indicates the median density, and the whisker shows ±1.53 interquartile range. ND, n = 13; T2D, n = 16. **p < 0.05, **p < 0.01, ***p < 0.001, ****p < 0.0001. Mann-Whitney U test.

Figures S2 and S3.

Author Manuscript Author Manuscript Author Manuscript Author Manuscript

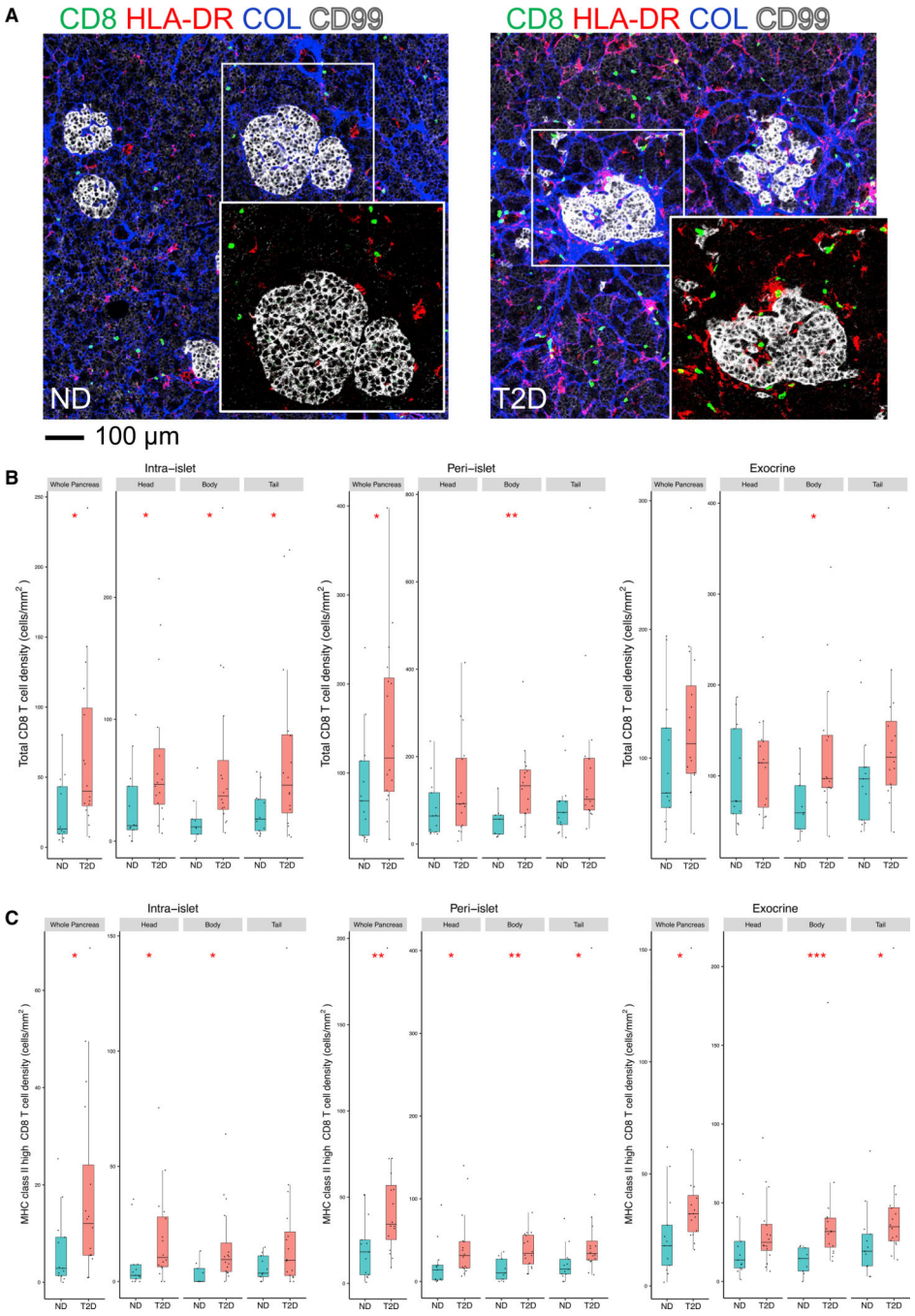

Figure 3. Intra-islet CD8 T and CD8/HLA-DR^{high} T cell density are increased in T2D

(A) CD8 T cell and HLA class II expression in the pancreas of ND (left) and T2D (right) organ donors. CD68 (green), HLA-DR (red), collagen (blue), and CD99 (white). The zoomed-in image is 1.5-fold of the original image.

(B) Boxplots showing total CD8 T cell density intra-islet, peri-islet, or in the exocrine pancreas. Data are presented for the whole pancreas and separately for head,body, and tail of the organ. Each dot represents the mean density of each donor. The black line inside of the

Author Manuscript Author Manuscript Author Manuscript Author Manuscript

boxplot indicates the median density, and the whisker shows ±1.5× interquartile range. ND, n = 13; T2D, n = 16. *p < 0.05. Mann-Whitney U test.

(C) Boxplots showing CD8/HLA-DR^{high} CD8 T cell density intra-islet, peri-islet, or in the exocrine pancreas. Data are presented for the whole pancreas and separately for head, body, and tail of the organ. Each dot represents the mean density of each donor. The black line inside of the boxplot indicates the median density, and the whisker shows ± 1.5× interquartile range. ND, n = 13; T2D, n = 16. *p < 0.05, **p < 0.01. Mann-Whitney U test. See also Figure S5.

Author Manuscript Author Manuscript Author Manuscript Author Manuscript

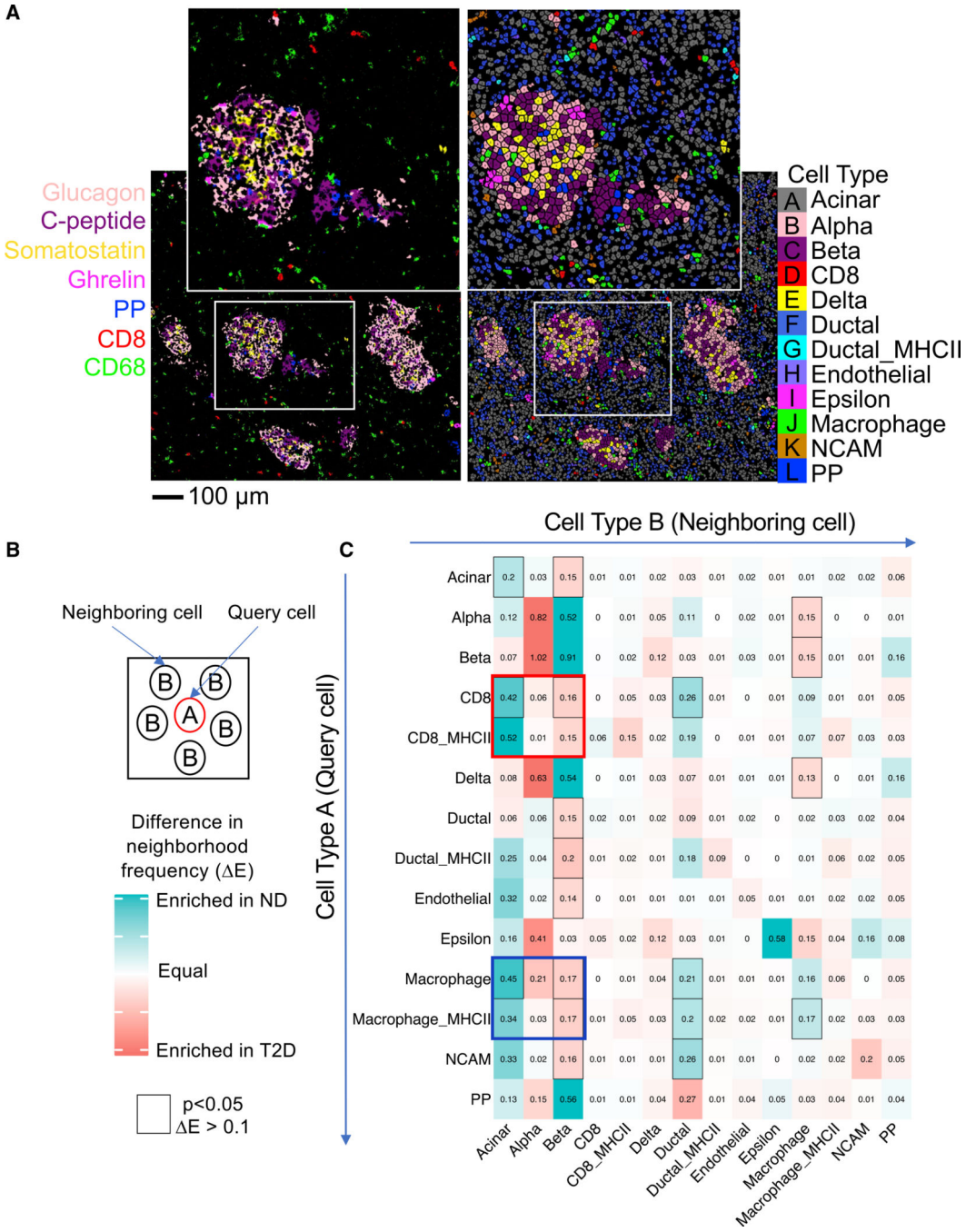

Figure 4. Neighborhood analysis

(A) Cell type annotation of the 14 major cell types determined after image segmentation was projected back to assemble the tissue map shown on the right. Note the close match to the original IMC image shown on the left, confirming the cell type annotation pipeline. The zoomed-in image is 2-fold of the original image.

(B) Principle of neighborhood analysis. For any cell “A,” termed query cell, the cell types of the adjacent cells (neighboring cells, “B”) were counted and summarized as a frequency matrix. Enrichment scores were calculated by comparing the observed frequency to the

Author Manuscript Author Manuscript Author Manuscript Author Manuscript

expected frequency obtained from randomizing cell labels for 100 rounds. Enrichment scores were then compared for statistical significance between control (n = 13) and T2D (n = 16) by permutation test.

(C) Heatmap displaying cell-cell interaction frequencies between control and donors with T2D. Statically significant results with Benjamini-Hochberg adjusted a p value of <0.05, and differences in enrichment scores of >0.1 are outlined by black boxes. Teal color indicates interactions that are more frequent in ND, and red indicates those that are more abundant in the patients with T2D. The red box highlights the finding that the presence of CD8 T cells near beta cells is more likely in the T2D pancreas, whereas the blue box emphasizes the point that macrophage/beta cell interactions are more likely in T2D than in the ND pancreas. See also Figure S4.

Author Manuscript Author Manuscript Author Manuscript Author Manuscript

KEY RESOURCES TABLE

REAGENT or RESOURCE	SOURCE	IDENTIFIER
Antibodies		
141Pr-HLA-ABC (Clone EMR8–5)	BD Biosciences	Cat#565292
142Nd-CD57 (Clone HCD57)	Fluidigm	Cat#3142007B
143Nd-CD31 (Clone C31.3+C31.7+C31.10)	LifeSpan BioSciences	Cat#LS-C390863–100
144Nd-CD14 (Clone EPR3653)	Fluidigm	Cat#3144025D
145Nd-C-peptide (Clone 3A1)	Thermo	Cat#MA1–22710; RRID: AB_558517
146Nd-Nestin (Clone 196908)	Fluidigm	Cat#3146015B
147Sm-Glucagon (Clone C-11)	Santa Cruz	Cat#sc-514592; RRID: AB_2629431
148Nd-Pan-Keratin (Clone C11)	Fluidigm	Cat#3148020D
149Sm-CD11b (Clone EPR1344)	Fluidigm	Cat#3149028D
150Nd-CD44 (Clone IM7)	Fluidigm	Cat#3150018B
151Eu-PDX1	R&D systems	Cat#AF2419; RRID: AB_355257
152Sm-CD45 (Clone 2B11)	Fluidigm	Cat#3152016D
153Eu-CD56	Proteintech	Cat#14255–1-AP; RRID: AB_2149421
154Sm-Beta-actin (Clone 2F1–1)	Fluidigm	Cat#3154021D
155Gd-FoxP3 (Clone 236A/E7)	Fluidigm	Cat#3155016D
156Gd-CD4 (Clone EPR6855)	Fluidigm	Cat#3156033D
158Gd-NKX6.1	Sigma	Cat#HPA036774; RRID: AB_10673664
159Tb-CD68 (Clone KP1)	Fluidigm	Cat#3159035D
160Gd-Somatostatin (G-10)	Santa Cruz	Cat#sc-13099; RRID: AB_2195930
161Dy-CD20 (Clone H1)	Fluidigm	Cat#3161029D
162Dy-CD8 (Clone C8/144B)	Fluidigm	Cat#3162034D
164Dy-CD99	R&D systems	Cat#AF3968; RRID: AB_2076301
165Ho-CA2	Rockland	Cat#200–401-136S; RRID: AB_2612117
166Er-NF-κB (Clone K10895.12.50)	Fluidigm	Cat#3166006A
167Er-Granzyme B (Clone EPR20129–217)	Fluidigm	Cat#3167021D
168Er-Ki67 (Clone B56)	Fluidigm	Cat#3168022D
169Tm-Collagen Type 1	Fluidigm	Cat#3169023D
170Er-CD3	Fluidigm	Cat#3170019D
171Yb-p16 (Clone 2D9A12)	Abcam	Cat#ab54210
172Yb-pS6 (Clone N7–548)	Fluidigm	Cat#3172008A
173Yb-CD45RO (UCHL1)	Fluidigm	Cat#3173016D
174Yb-HLA-DR (Clone TAL 1B5)	Abcam	Cat#ab20181; RRID: AB_445401
175Lu-Pancreatic Polypeptide	Abcam	Cat#ab77192; RRID: AB_1524152
176Yb-Ghrelin	Santa Cruz	Cat#sc-10368; RRID: AB_2232479
Biological samples		
organ donor pancreas tissue blocks	The Human Pancreas Analysis Program, https://hpap.pmacs.upenn.edu/	RRID:SCR_016202

Author Manuscript Author Manuscript Author Manuscript Author Manuscript

REAGENT or RESOURCE	SOURCE	IDENTIFIER
organ donor pancreas tissue blocks	nPOD; https://www.jdrfnpod.org/	RRID:SCR_014641
Software and algorithms		
MCD Viewer 1.0.560.6	Fluidigm	https://www.fluidigm.com/software
R version 4.0.2 (2020–02–29)		http://www.R-project.org/
Fiji	Schindelin et al., 2012	https://imagej.net/software/fiji
Ilastik 1.3.3	Berg et al., 2019	https://www.ilastik.org
Cellprofiler 3.1.9	Carpenter et al., 2006	https://cellprofiler.org
Custom CellProfiler plugins	Zanotelli et al., 2020	https://github.com/BodenmillerGroup/ImcPluginsCP
EBImage 4.30.0	Pau et al., 2010	https://github.com/aoles/EBImage
CATALYST 1.12.2	Chevrier et al., 2018	https://github.com/HelenaLC/CATALYST
FlowSOM	Van Gassen et al., 2015	https://github.com/SofieVG/FlowSOM
neighborhood Version 0.3.0	Schapiro et al., 2017	https://github.com/BodenmillerGroup/neighbouRhood
Other		
Image data	This paper	N/A
Analyses released on https://github.com/Kaestner-Lab/T2D_IMC	This paper	https://doi.org/10.5281/zenodo.5557120